ACS APPLIED MATERIALS & INTERFACES

www.acsami.org Research Article

Lithium Pyrene Squarate Covalent Organic Frameworks for Efficient Lithium and Magnesium Separation from Salt Water

Ataf Ali Altaf, Ahmadreza Khosropour, Amin Zadehnazari, and Alireza Abbaspourrad*

Cite This: https://doi.org/10.1021/acsami.3c01051 Read Online

ACCESS | Metrics & More | Article Recommendations | Supporting Information

ABSTRACT: The increasing pressure for lithium resources from the electric vehicle and nuclear energy industries means that new technologies to separate Mg^{2+} from Li^+ from salt water are in demand. To address this need, we fabricated lithium pyrene squarate covalent organic frameworks (Li-SQCOFs) to separate Mg^{2+}/Li^+ mixtures from salt water. We optimized the effect of the electrolyte and the amount of the adsorbent and then carried out a kinetics study on the adsorbent recovery at various pH levels using both batch and continuous flow adsorption methods. Li-SQCOF was found to have excellent selectivity for solutions containing a mixture of Mg^{2+}/Li^+ ions. This work represents a unique path for the separation of Mg^{2+}/Li^+ through direct adsorption using a covalent organic framework (COF). The COF-supported ultrafiltration bed made in this study gave a Mg^{2+} separation flux of 60.5 h^{-1} m^{-2}.

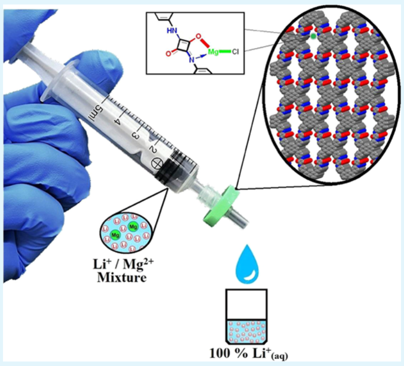

KEYWORDS: *covalent organic frameworks, ultrafiltration, lithium ion, magnesium ion, selective separation*

1. INTRODUCTION

The consumption of lithium resources is expected to rise rapidly and continuously due to the growing worldwide market demand for Li-ion batteries and nuclear power plants.[1−3] The concern over the depletion of lithium ores has prompted research into lithium-ion recovery from a wide variety of sources.[4−6] When compared to hard rock ore mining, Li-salt extraction from brine is easier, more environmentally friendly, and less expensive.[7] Recent efforts have been made to find efficient and scalable methods to recover Li^+ ions from salt water; in particular, salt water lakes in South Africa.[8]

The foremost challenge for recovering Li^+ ions from salt-lake brines is separating them from Mg^{2+} ions, which have similar properties like ionic radius and chemical reactivity.[9,10] The techniques currently used for Li^+ mining from salt-lake brines containing high Mg^{2+}-to-Li^+ ratios include calcination, adsorption, and extraction.[11] Various membrane-based technologies like membrane electrodialysis, reverse osmosis, liquid-based or supported membranes, and nanofiltration methods have been investigated to separate Mg^{2+} and Li^+ ions from each other. The current state-of-the-art methods for the separation of Mg^{2+}/Li^+ require large amounts of harmful and corrosive chemicals, produce significant waste materials, and are energy-intensive throughout the process.[12−14] Finding a sustainable solution to separate the two similar ions while using less solvent and producing less waste is desirable.

Covalent organic frameworks (COFs) are a family of polymeric porous and crystalline materials with high surface area, chemical stability, and significant adsorption capabilities that make them attractive in water decontamination applications.[15−18] COFs are synthesized from various molecular building blocks, and the synthetic methods are designed to generate specific structural attributes such as tunable pore sizes and shapes.[19] Further, COFs have been found to be excellent adsorbent materials while maintaining their crystallinity and porosity.[20] The adsorption properties of COFs have made them promising materials for gas separation[21] and molecular separation in liquids.[22] Most COFs have intrinsic pore sizes in the range of 1−3 nm, which makes them suitable for dye separation applications.[23−25] Applying the tenets learned from dye separation technology and considering the tunable nature of the pore size, the foundation for using COF membranes for the removal of specific ions from water has been established. Therefore, COFs have potential as primary components for membranes for desalination.[26−28] Although membrane technology using COFs or MOFs has already shown great success in separating Mg^{2+}/Li^+ mixtures,[29−31] big challenge remains for the removal of small traces of Mg^{2+} in the resulting mixture of Mg^{2+}/Li^+ from initial separations. The other challenges associated with membrane technology are membrane fabrication and separation conditions: the fabrication currently uses a tedious process to monitor the porosity of the membrane; and the separation

Received: January 23, 2023
Accepted: March 27, 2023

Scheme 1. Synthetic Scheme for the Lithium Pyrene Squarate Covalent Organic Framework (Li-SQCOF)

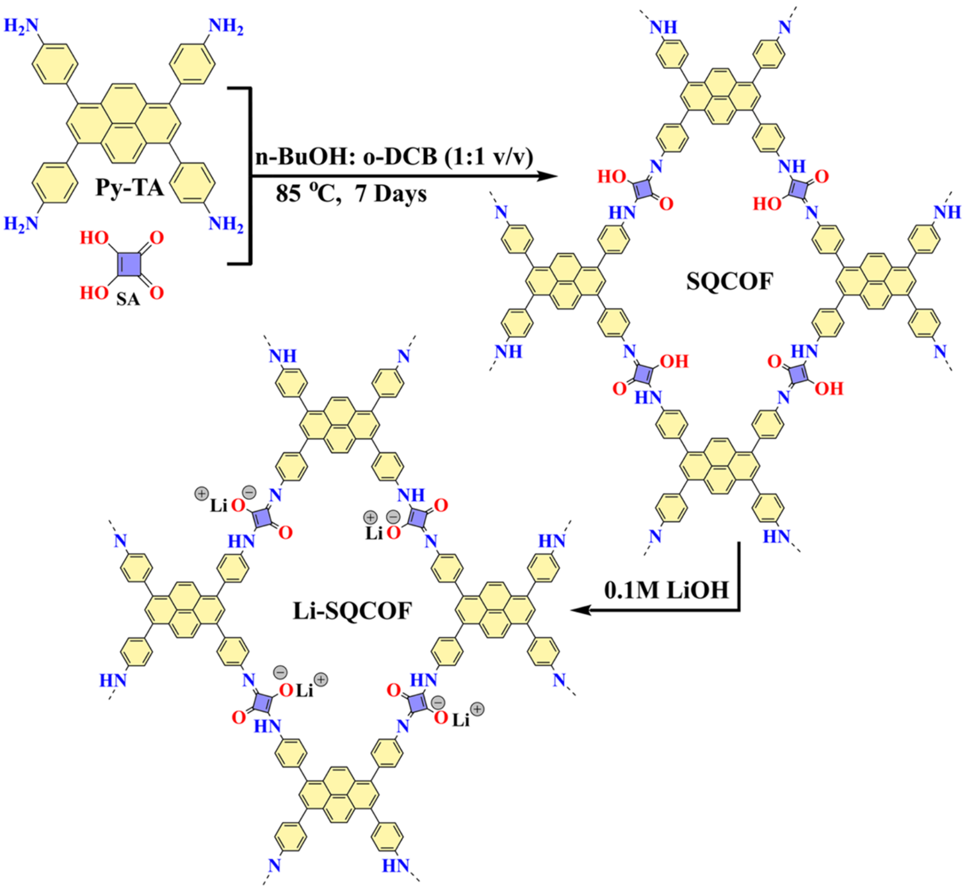

conditions require precise control of the electric potential. Thus, facile manufacturing of the separation materials, methods to completely remove the Mg^{2+}, specifically from Mg^{2+}/Li^{+} mixtures, and a simple process for selective adsorption of Mg^{2+} are sought.

To address the need for a low-cost, low-energy, and environmentally-friendly method for the separating of Li^{+} from Mg^{2+}, we investigated the selective adsorption of Mg^{2+} from Li^{+}/Mg^{2+} mixtures with a lithium pyrene squarate COF (Li-SQCOF) (Scheme 1). Our Li-SQCOF showed preferential adsorption of Mg^{2+}, and we optimized the conditions for this adsorption by studying the effects of the amount of COF needed, types of electrolytes, solution contact time with the COF, and the reusability for the adsorption at different pH levels using both batch and continuous flow adsorption processes.

2. EXPERIMENTAL SECTION

2.1. Materials. Squaric acid (SA, 98%, Matrix Scientific), 1,3,6,8-tetrabromopyrene (97%, Chemscene), n-butanol (n-BuOH, anhydrous 99.98%, Sigma-Aldrich), acetone (99.5%, Fischer Chemicals), o-dichlorobenzene (DCB, 99%, Alfa Aesar), *N,N*′-dimethylformamide (DMF, anhydrous 99.8%, Sigma-Aldrich), tetrahydrofuran (THF, HPLC Grade, Tedia High Purity Solvents), lithium chloride (Fisher Scientific, 99.9%), magnesium sulfate (98%, Sigma-Aldrich), hydrochloric acid (36.5−38.0%, Sigma-Aldrich), lithium hydroxide (98%, Sigma-Aldrich), potassium chloride (KCl, ACS reagent, 99.0−100.5%, Sigma-Aldrich), and sodium chloride (ACS reagent, ≥99.0%, Sigma-Aldrich) were used as received. The synthesis of 4,4′,4″,4‴-(pyrene-1,3,6,8-tetrayl)tetraaniline (Py-TA) was carried out according to a previously reported procedure.[32]

Solid-state nuclear magnetic resonance (SSNMR) measurements were made on a Bruker Avance-III-HD-ss500 spectrometer (analysis parameters: ^{13}C-CPMAS; relaxation delay-5s; Scans-12k and 12 KHz of magic angle spinning). Powder X-ray diffraction (PXRD) analysis was done on a Bruker D8 powder diffractometer with nickel-filtered Cu Kα radiation at 40 kV and 100 mA. For PXRD simulations, CrystalMaker and CrystalDiffract software were used, CrystalMaker Software Ltd, Oxford, England (www.crystalmaker.com). Field emission scanning electron microscopy (SEM) was carried out using a Zeiss LEO 1550 FESEM, and transmission electron microscopy (TEM) was done on an FEI/Thermo Fisher Titan Themis CryoS/TEM 60-300 kV. X-ray photoelectron spectroscopy (XPS) samples were analyzed using a Scienta Omicron ESCA-2SR with an operating pressure of ca. 1×10^{-9} Torr. Monochromatic Al Kα X-rays (1486.6 eV) were generated at 250 W (15 kV; 20 mA) with photoelectrons collected from a 2 mm diameter analysis spot. and Fourier transform infrared spectroscopy (FTIR) was done on a Thermo Scientific Nicolet iN5 and was used to analyze the surface compositions of synthesized COF materials. Inductively coupled plasma (ICP) atomic emission spectroscopy was carried out on ICP-OES by Spectro Analytical Instruments, Inc, and the EPA 6010-B method was used for analysis (https://www.epa.gov/sites/default/files/documents/6010b.pdf).

2.2. Synthesis of Li-SQCOF. The pyrene squaric acid-based COF (SQCOF) was synthesized by following the synthetic procedures reported with some modifications; details can be found in the Supporting Information (Scheme 1).[33] To make the Li-SQCOF, the dried SQCOF (200 mg) was treated with 10 mL of aqueous 0.1 M LiOH for 6 h, followed by 30 min of sonication at 35 kHz. The bright orange solid was then filtered and washed with water until the filtrate was pH neutral.

2.3. Separation of Cations. Stock solutions, 500 mg L^{-1} of each Mg^{2+} and Li^{+}, were prepared by dissolving $MgSO_4 \cdot 7H_2O$ (2.54 g, 10.3 mmol) and $LiCl \cdot H_2O$ (2.18 g, 36.0 mmol) in 500 mL of deionized

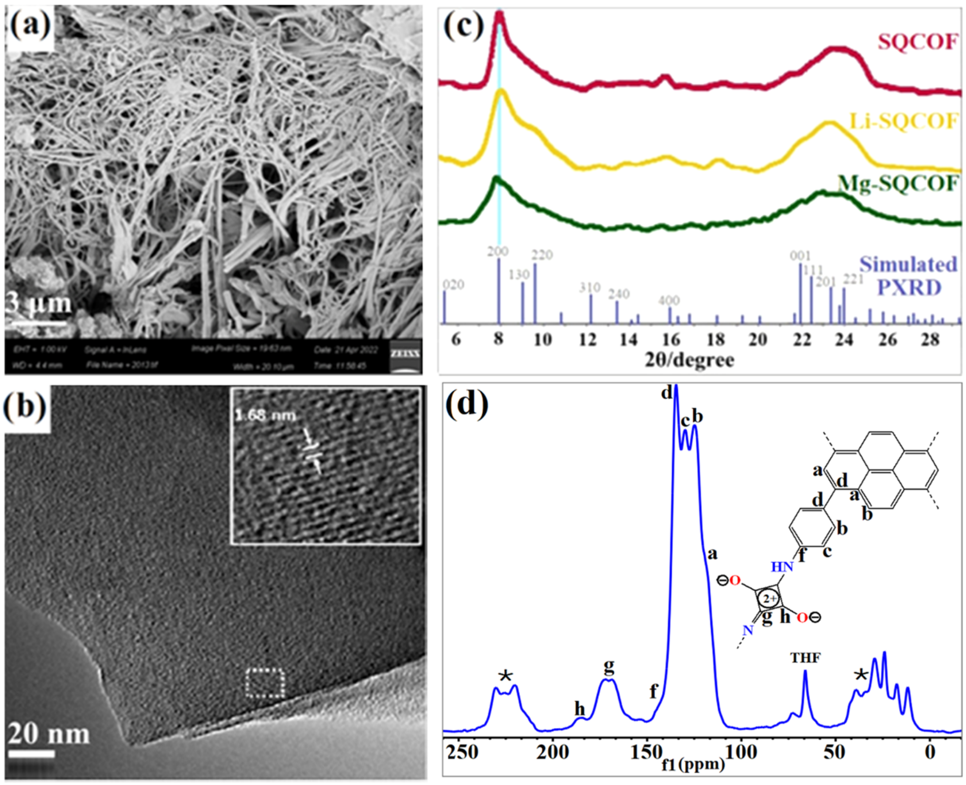

Figure 1. (a) SEM image for the morphology of SQCOF in the eclipsed conformer, (b) HRTEM image of SQCOF, (c) PXRD patterns of SQCOF, Li-SQCOF, and after Mg^{2+} capture (Mg-SQCOF) along with the simulated PXRD pattern, and (d) CP/MAS ^{13}C NMR spectra of SQCOF; THF was used to wash the product during purification.

water (18.2 MΩ cm deionized with a Milli-Q IQ 7000 Ultrapure Water System). Different dilutions of Mg^{2+}, Li^{+}, and Mg^{2+}/Li^{+} mixtures were made in deionized water.

Batch separations were carried out in a test tube. Solid SQCOF or Li-SQCOF (~1 to 30 mg) was added to the tube, followed by ~8 to 12 mL of cation solutions. The tube was either shaken or sonicated for 30 min. The solution was then filtered through a syringe filter (Whatman HPLC syringe filter, 7 mm, Teflon/nylon, 0.2 μm), and the filtrate was analyzed by ICP atomic emission spectroscopy.

Continuous flow adsorption separations were carried out using a 30 mm diameter filtration bed made on a Whatman filter paper (Spartan 30/0.22) with a 0.22 μm pore size. A water suspension of SQCOF or Li-SQCOF (30 mg) was injected into the filter and allowed to settle on the surface of the filter paper inside the syringe filter. An injection flow pump (Fusion 200) was used to maintain a constant flow rate of 900 mL h^{-1}. The estimation of both cations (Mg^{2+} and Li^{+}) was performed on ICP atomic emission spectroscopy (Figure S2).

3. RESULTS AND DISCUSSION

3.1. Synthesis and Characterization of SQCOF and Li-SQCOF.

The synthesis of SQCOF has been reported in the literature, and its crystallinity was shown to be dependent on the ratio of squaric acid to Py-TA.[33] Further, Ding et al. reported that using a 1:1 mixture of mesitylene and dioxane as the solvent system exclusively formed the 1,3-isomer of the squaric acid connector.[33] In the same report, they noted that when DCB/n-BuOH was used as the solvent system, the 1,2-isomer was produced. In our synthetic study, we used an excess of squaric acid and DCB/n-BuOH as the solvent, and our SSNMR, FTIR, and PXRD data indicate that we have exclusively produced the 1,3-isomer of the squaric acid connector (Figure 1).[33] The formation of the 1,3-isomer in our case is likely due to the slight differences in our synthetic procedure, which include the absence of water and lower reaction temperature. Other reports where squaric acid is used as a connector also conflict. Some report a 1,2-coupling product or a mono-substitution of the squaric acid in the presence of water and the protic acid catalyst,[34−39] while others suggest the 1,3-coupling[39,40] and some indicated the isomer formed was independent of the solvent system entirely.[41,42] Therefore, because our experimental data most closely match that of the 1,3-isomer reported by Ding et. al., we are reasonably confident that is what we have produced in our synthesis.

SQCOFs, before and after the Mg^{2+} adsorption activity, were characterized by powder X-ray diffraction (PXRD) analysis. The SQCOF before Mg^{2+} adsorption activity showed high crystallinity and reasonably good chemical stability after Mg^{2+} adsorption, which is evident from the PXRD patterns. The PXRD simulation studies indicate that SQCOF has a $P2/m$ space group in a monoclinic crystal system ($a = 23.97$, $b = 36.06$, $c = 3.46$ Å, $\gamma = 91.46°$) that is in good agreement with the literature.[33] The simulated PXRD pattern has shown the characteristic 2θ peaks at 7.85, 9.58, 15.90, 21.87, 22.42, 23.33, and 24.02° values, which correspond to the miller indices (hkl) 200, 220, 420, 001, 111, 201, and 221 respectively (Figure 1c). The signal at 7.85 indicates that SQCOF retains its crystallinity after the formation of Li-SQCOF and Mg-SQCOF. The SEM image shows a fibrous network-type morphology for the eclipsed conformer of SQCOF (Figure 1a), and the HRTEM image indicates that the interlayer distance is 1.68 nm (Figure 1b) that belongs to the 020 face of the crystal unit cell.

SSNMR ^{13}C CP/MAS spectra confirmed the formation of the 1,3-isomer of the SQCOF structure (Figure 1d). The presence of the SQ linker was confirmed by the peak at 187 ppm that

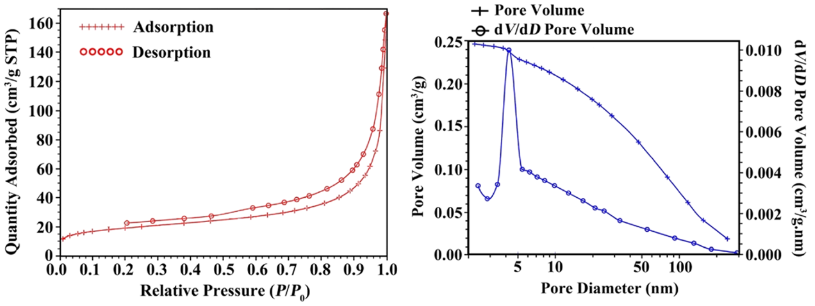

Figure 2. BET surface area analysis plot (left) and pore size estimation plot (right).

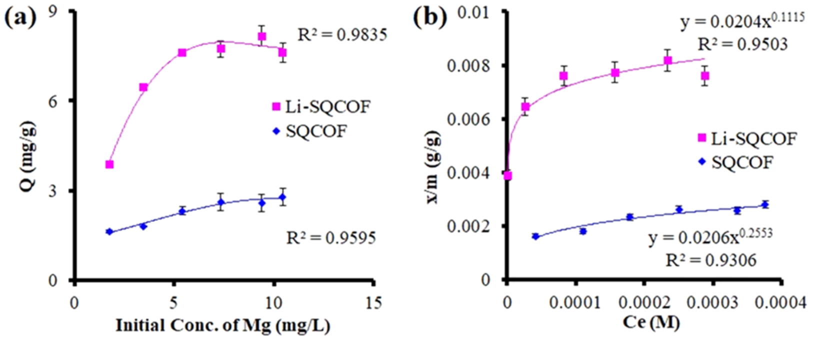

Figure 3. (a) Mg^{2+} adsorption capacity of SQCOF and Li-SQCOF as a function of initial Mg^{2+} concentration. (b) Freundlich adsorption isotherms for SQCOF and Li-SQCOF.

Table 1. Adsorption Capacity (Q) of SQCOF for Mg^{2+} and Li^{+} in Salt Water Containing Variable Concentrations of Mg^{2+} and Li^{+}

sr. no.	starting conc. of Mg^{2+} (mg L^{-1})	starting conc. of Li^{+} (mg L^{-1})	Q for Mg^{2+} (mg g^{-1}) ± St. Dev.	Q for Li^{+} (mg g^{-1}) ± St. Dev.
1	50.00		3.30 ± 0.16	
2		50.00		0.15 ± 0.04
3	50.00	50.00	3.60 ± 0.11	0.12 ± 0.04
4	50.00	5.00	3.37 ± 0.16	0.03 ± 0.02
5	5.00	50.00	3.30 ± 0.34	0.14 ± 0.03
6	5.00	5.00	3.10 ± 0.26	0.04 ± 0.02
7	5.00		2.94 ±0. 22	

corresponds to the quaternary C of the carbonyl group C−O (h in Figure 1d) and C−N carbons of the four-membered ring at 176 ppm (g in Figure 1d). The other aromatic carbons appear in the range of 118−142 ppm (a, b, c, d, and f in Figure 1d). The signals between 160 and 170 ppm confirm the 1,3-isomer, as the increased symmetry of the 1,2-isomer would result in a loss of signals between 160 and 170 ppm.

The FTIR spectra of SQCOF before and after the Mg^{2+} separation activity shows the expected changes (Figure S3). The band at 3304 cm^{-1}, attributed to the hydroxyl groups in the parent compound, disappears upon addition of Mg^{2+} when the protons are replaced with Mg^{2+}. The carbonyl stretch appears at 1700 and 1795 cm^{-1}, and the C═C aromatic stretching at 1394 cm^{-1}. The weak vibrations around 3250 cm^{-1}, attributed to N−H stretching, are still present but less intense upon interaction with the Mg^{2}.

The specific surface area of SQCOF was calculated by multipoint BET surface area analysis (Figure 2). The specific surface area of SQCOF was 70 m^{2} g^{-1}, whereas the value of constant C for SQCOF was 185, which indicates the microporous characteristics; $C > 150$ is considered microporous.[43] The pore size distribution curve indicated the smallest pore in the SQCOF as 19.4 nm. High surface area and porosity are good indicators for its use as an adsorbent in batch, as well as continuous flow, systems.

3.2. Mg^{2+} Adsorption Activity.

After the characterization of the SQCOF and Li-SQCOF, the adsorption selectivity toward Mg^{2+} was evaluated as a low-cost, low-energy, and environmentally-friendly method for the separation of Li^{+} from Mg^{2+}. Using batch separation conditions, solutions of various concentrations of Mg^{2+}, Li^{+}, and mixtures of both were treated with solid COF, and the filtrate was analyzed by ICP atomic emission spectroscopy. The adsorption capacity of the SQCOF for Li^{+} and Mg^{2+} under different concentrations of Li^{+} and Mg^{2+} was determined using the following equation[44]

$$Q = \frac{(C_0 - C)V}{m} \tag{1}$$

where Q (mg g^{-1}) is the adsorption capacity, C_0 (mg L^{-1}) is the initial Mg^{2+} concentration, C (mg L^{-1}) is the remaining Mg^{2+} concentration in the supernatant, V (L) is the volume of the initial solution, and m (g) is the amount of the adsorbent. The adsorption capacity (Q) of SQCOF for Mg^{2+} and Li^{+} in separate and mixed solutions of Mg^{2+} and Li^{+} shows that SQCOF adsorption is highly selective toward Mg^{2+} (Figure 3 and Table 1). Different concentrations were tested to check the adsorption capacity of SQCOF in different concentrations as a preliminary

https://doi.org/10.1021/acsami.3c01051
ACS Appl. Mater. Interfaces XXXX, XXX, XXX−XXX

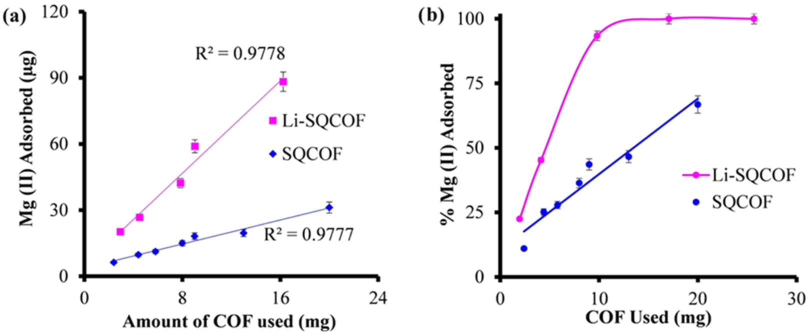

Figure 4. Effect of the adsorbent (SQCOF and Li-SQCOF) amount on (a) Mg^{2+} adsorption and (b) Mg^{2+} adsorption in the presence of Mg^{2+} (4.00 mg L^{-1}) and Li^+ (50.00 mg L^{-1}) in salt water; no remarkable change in Li^+ concentration was observed.

test. For the solutions of Mg ions, we found Q to be 2.94 mg $g^{-1}$for 5.00 mg L^{-1} ion solutions and 3.30 mg g^{-1} for 50.0 mg L^{-} ion solutions, indicating similar adsorption capacities. However, low adsorption was observed for Li^+ (0.15 mg g^{-1} for a 50.0 mg L^{-1} solution), which was further decreased for a 5.00 mg L^{-1} solution of Li^+. For the mixed ion solutions, Q_s values of 3.60 mg g^{-1} for Mg^{2+} and 0.12 mg g^{-1} for Li^+ were observed for the 50.0 mg L^{-1} solution, which indicated the selectivity of the SQCOF toward Mg^{2+} ions. A similar pattern was observed for the lower-concentration solution of the mixed ions (5.00 mg L^{-1}). Q was found to be 3.30 mg g^{-1} for Mg^{2+}, and a slight amount of Li^+ was captured by SQCOF.

Adsorption capacities of SQCOF were also calculated for mixture solutions containing 50 mg L^{-1} Mg^{2+} and 5.00 mg L^{-1} of Li^+ concentration and vice versa. For both mixture solutions, selective removal of Mg^{2+} was observed (Table 1).

Due to the different binding affinities of Li^+ and Mg^{2+} by SQCOF, XPS analysis was used to evaluate the interaction between Mg^{2+} ions and SQCOF. The coordination of Mg^{2+} by nitrogen was confirmed by X-ray photoelectron spectroscopy (XPS, Figure S4). Adsorption of Mg^{2+} is likely due to the replacement of protons from the squaric acid connector along with the coordination of nitrogen from the SQCOF backbone (Scheme S1). The XPS spectra of SQCOF and Mg-SQCOF are presented in Figures S4 and S5. The peaks for Mg-SQCOF were slightly shifted to higher binding energies. The O atoms shifted from 531 to 533 eV with the appearance of a shoulder around 536 eV, indicating two possible bonding interactions of oxygen. The N atoms in Mg-SQCOF also show a higher energy shift from 399 to 403 eV with a small shoulder around 398 eV.

To improve the adsorption of Mg^{2+}, SQCOF was treated with LiOH to deprotonate the squarate linker and increase the negative surface charge. The observed ζ potential for SQCOF before LiOH treatment was 11.66 mV, whereas after treatment with LiOH, the deprotonated Li-SQCOF exhibited a negative surface charge of −35.33 mV. The adsorption capacity toward Mg^{2+} after LiOH treatment was measured for Mg^{2+}, Li^+, and Mg^{2+}/Li^+ mixed solutions. Li-SQCOF had more than twice the adsorption capacity of SQCOF (Figure 3a).

3.3. Effect of the Mg^{2+} Concentration on Absorption Capacity (*Q*).

An increase in Mg^{2+} adsorption capacity was observed for the same mass of SQCOF and Li-SQCOF with increasing concentration of Mg^{2+}(Figure 3). For SQCOF with a 1.27 mg L^{-1} Mg^{2+} solution, the observed value of Q was 1.63 mg g^{-1}, which increased to 2.80 mg g^{-1} for a 10.45 mg L^{-1} solution. A similar ratio between the two concentrations was also observed for Li-SQCOF; however, Q was observed to be larger for both solutions, where Q was observed as 3.88 mg g^{-1} for the 1.27 mg L^{-1} Mg^{2+} solution and 7.60 mg g^{-1} for the 10.45 mg L^{-1} Mg^{2+} solution. This increase between the SQCOF and the Li-SQCOF toward Mg^{2+} indicated a greater efficiency for Mg^{2+} removal by the Li-SQCOF. This rise in Q for both the adsorbents (SQCOF and Li-SQCOF) with increasing concentration of adsorbate (Mg^{2+}) is in agreement with the Freundlich adsorption isotherm (Figure 3b) model eq (2).[45]

$$\frac{x}{m} = KC_e^{1/n} \qquad (2)$$

where x is the mass of Mg^{2+}, m is the mass of COF (SQCOF or Li-SQCOF), C_e is the equilibrium concentration of Mg^{2+}, *and* K and n are the constants. The value of K was found to be 0.0206 and 0.0204 for SQCOF and Li-SQCOF, respectively, whereas n was calculated to be 3.92 and 8.97 for SQCOF and Li-SQCOF, respectively. The higher value of n for Li-SQCOF indicates the availability of more adsorption sites.[46] This increase may be ascribed to hydrated ionic diameters of metal ions for alkali and alkaline earth metals and the order of transport rate for them, which is $Li^+ < Na^+ < K^+ < Mg^{2+}$. This order is the same as the order of their ionic conductivity in infinite dilution. The higher adsorption of Mg^{2+} on Li-SQCOF rather than on the SQCOF may be due to Mg^{2+} acting as a better Lewis acid with a lower transportation rate on the negative surface of Li-SQCOF in comparison to SQCOF; Li-SQCOF is more selective toward Mg^{2+}.[47]

3.4. Effect of the Adsorbent Amount on Absorption of Mg^{2+}.

Different masses of SQCOF and Li-SQCOF were used to investigate the effect of the mass of the adsorbent on Mg^{2+} ion removal at a constant concentration of 4.00 mg L^{-1}. A linear and dependent relationship was observed for Mg^{2+} capture using SQCOF and Li-SQCOF with respect to the amount of the adsorbent used (Figure 4). Overall, Li-SQCOF showed a steeper increase in the amount of Mg^{2+} that was captured than SQCOF. This increase in adsorption capacity observed for Li-SQCOF is attributed to the increased substrate surface that is available on Li-SQCOF. Mg^{2+} adsorption was higher for Li-SQCOF due to the slower transport rate of Mg^{2+} in the presence of more substrate ions. Nearly 100% Mg^{2+} adsorption was found using 10 mg of Li-SQCOF and afterward when the 4.00 mg L^{-1} Mg^{2+} solution was used. This confirmed the high selectivity and efficiency for the adsorption of Mg^{2+} at low concentrations.

3.5. Effect of Ionic Strength and Other Cations on Absorption of Mg^{2+}.

To evaluate the effect of different ions on the adsorption of Mg^{2+}at the Li-SQCOF surface, a constant concentration of Mg^{2+} (10.0 mg L^{-1}) was treated with a constant mass of the adsorbent (Li-SQCOF, 8.00 mg) in the presence of variable concentrations of KCl and NaCl solutions. The

https://doi.org/10.1021/acsami.3c01051

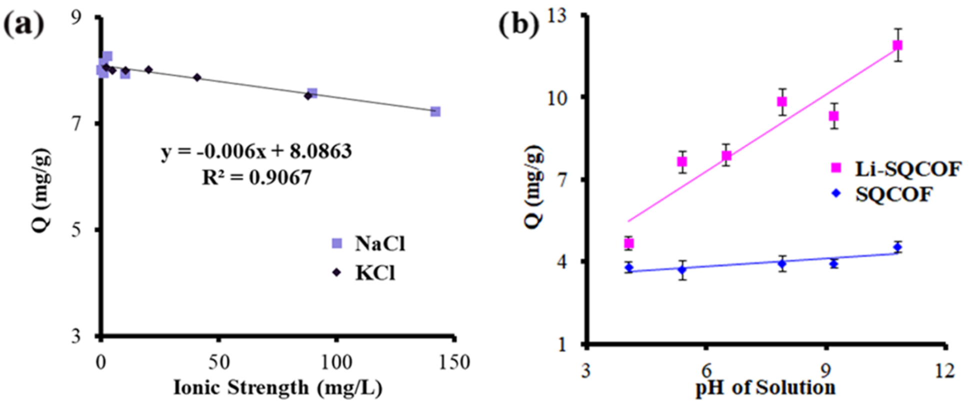

Figure 5. Effect of (a) ionic strength of electrolytes and (b) pH of the salt solution on the adsorption capacity of Mg^{2+}.

adsorption capacity was found to be 8.05 mg g^{-1} for Mg^{2+} in the presence of a 2.33 mg L^{-1} KCl solution, whereas in the presence of NaCl, a maximum adsorption capacity for Mg^{2+} of 8.27 mg g^{-1} was observed for the 2.40 mg L^{-1} solution, which slightly decreased with increasing ionic strength of solution. At the highest ionic strength (∼140 mg g^{-1}), the minimum adsorption capacity is 7.23 mg g^{-1}. For both solutions, a slightly decreasing linear trend was observed with the increasing ionic strength of the adsorbate solution (Figure 5a).

3.6. Effect of pH. To evaluate the effect of the pH of the salt solution on adsorption of Mg^{2+} on the SQCOF and Li-SQCOF surfaces, a constant concentration of Mg^{2+} was treated with a constant amount of adsorbent (SQCOF and Li-SQCOF) at variable pH levels (4.1, 5.4, 6.5, 7.9, 9.2, and 10.8). The pH of the solutions was maintained by the addition of HCl and NaOH as needed. A linear increasing trend was observed as the pH of the solution was increased for both COFs; however, in the case of Li-SQCOF, the adsorption capacity was higher to start, and it increased more significantly than for SQCOF (Figure 5b). In this case, the Q value increased from 3.70 mg g^{-1} (at pH 4.1) to 4.50 mg/g (at pH 10.8). Here, the value of Q increased from 4.70 mg g^{-1} (at pH 4.1) to 11.90 mg g^{-1} (at pH 10.8). This increase in adsorption capacity may be attributed to the deprotonation of SQCOF at higher pH, which facilitates the binding between Mg^{2+} and the resultant SQCOF surface. It is notable that the SQCOF at pH 10.8 is similar to the Li-SQCOF at pH 4.1, indicating that the absorption of Mg^{2+} increases with increasing deprotonation of SQCOF. The boost in the adsorption capacity of Li-SQCOF at higher pH levels may be due to its increased negative surface charge. At higher pH, the ζ potential of Li-SQCOF increases significantly, while the ζ potential of SQCOF approaches that of the Li-SQCOF at lower pH levels (Figure 6).

3.7. Adsorption Kinetics. To evaluate the kinetics of Mg^{2+} adsorption, Mg^{2+} removal in the presence of Li^+ was evaluated over time. Instant selective adsorption of Mg^{2+} from the mixture in the first minute was studied for SQCOF as well as Li-SQCOF (Figure 7). For SQCOF, 2.2 mg g^{-1} Mg^{2+} was adsorbed in 3 min, and after 63 min, the adsorption increased to 3.4 mg g^{-1}, whereas in the case of Li-SQCOF, 4.99 mg g^{-1} Mg^{2+} was adsorbed within 1 min. After 3 min, 6.70 mg g^{-1} was absorbed with no further significant change. The 1 min Mg^{2+} adsorption trend is attributed to the maximum population of Mg^{2+} ions that could be absorbed onto the surface of Li-SQCOF. The slowing and subsequent plateauing of Mg^{2+} adsorption were attributed to the decreased availability of surface sites.[48] The adsorption of Mg^{2+} on the SQCOF and Li-SQCOF surfaces followed the pseudo-second-order (PSO) kinetic model by following eq (3).[49]

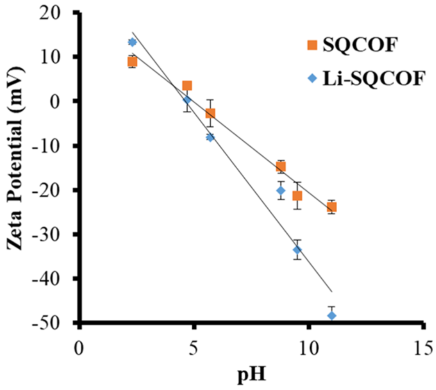

Figure 6. ζ Potentials for SQCOF and Li-SQCOF as a function of pH.

$$\frac{t}{q_t} = \frac{1}{kq_e^{2}} + \frac{t}{q_e} \qquad (3)$$

where q_t is the concentration of the adsorbate at time (t), q_e is the equilibrium concentration, and k is the PSO rate constant. The values of q_e and k were calculated from the slope and intercept, respectively, when t/q_t is plotted against t (Figure 7b). The values of k for SQCOF and Li-SQCOF were found to be 0.027 and 0.073 L mol^{-1} s^{-1}, respectively. The values of q_e were found to be 4.58 and 6.28 mg g^{-1} for SQCOF and Li-SQCOF, respectively.

3.8. Desorption Kinetics. After evaluating the pH stability of SQCOF via PXRD (Figure S6), the recovery of the adsorbent was investigated by treating the used adsorbent with HCl between runs to extract Mg^{2+} and regenerate the adsorbent. The Mg^{2+}-SQCOF was treated with HCl, keeping the pH constant at pH 3.0, and the Mg^{2+} release was quantified at different time intervals. After 30 min, 1.80 mg L^{-1} Mg^{2+} was recovered from Mg-SQCOF (21 mg, Figure 8a). The Mg^{2+} release became nearly linear after 30 min, and after 2 h, the optimal recovery of SQCOF was achieved.

Desorption kinetics for SQCOF in HCl was also best represented by the pseudo-second-order kinetic model (eq 3), the rate constant for Mg^{2+} recovery from Mg-SQCOF was found as 0.044 L $mol^{-1}s^{-1}$ with an R^2 value of 0.9999 (Figure 8a), and q_e was calculated as 4.73 mg g^{-1} in this case.

The samples of Mg-SQCOF produced from the adsorption of SQCOF and Li-SQCOF were treated as two different types of

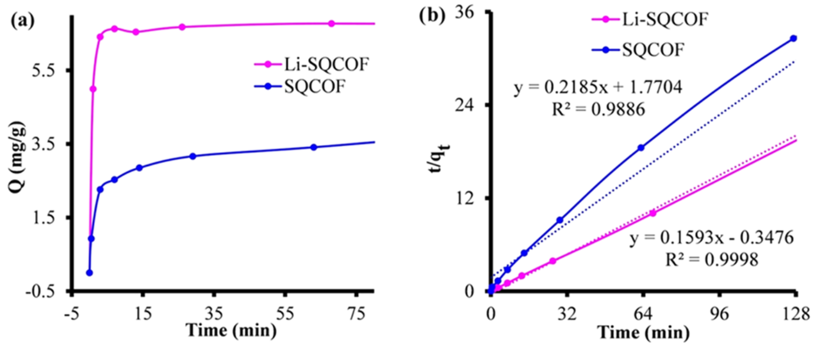

Figure 7. (a) Effect of time on Mg^{2+} adsorption by SQCOF and Li-SQCOF, and (b) the plot of t/q_t against t for the calculation of the rate constant.

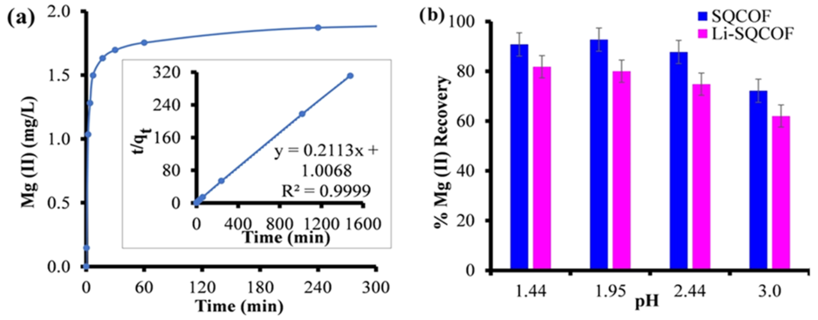

Figure 8. (a) Percentage of Mg^{2+} recovery using HCl at pH 3.0 from SQCOF at different time intervals; pseudo-second-order kinetics of Mg^{2+} recovery by SQCOF (inset), (b) Effect of different pH values on the percentage recovery of Mg^{2+} from SQCOF and Li-SQCOF.

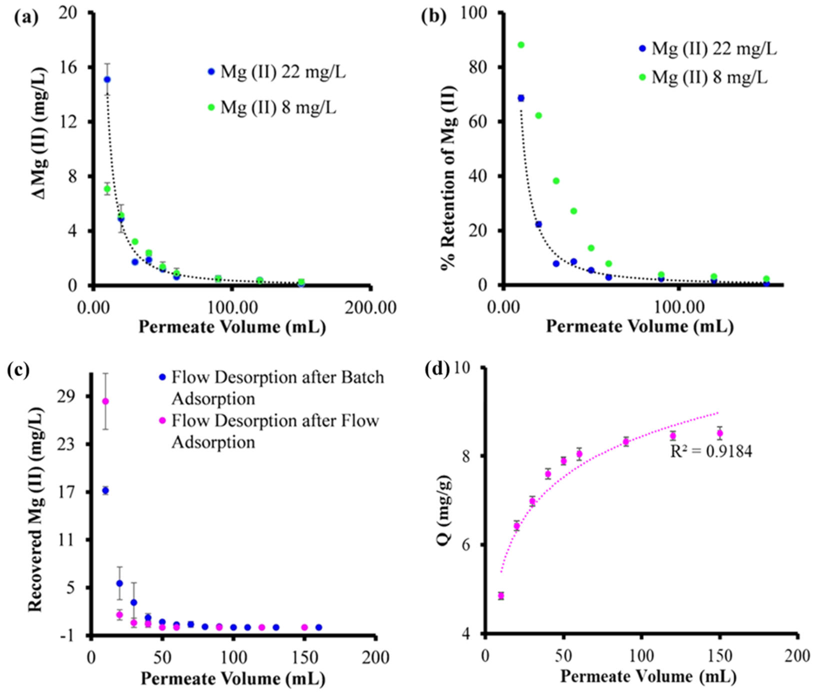

Figure 9. Mg^{2+} adsorption activity by Li-SQCOF under a continuous adsorption system using 22 and 8 mg L^{-1} Mg^{2+} permeate solutions. (a) Change in Mg^{2+} concentration under flow. (b) % Removal of Mg^{2+} by Li-SQCOF under flow. (c) Mg^{2+} (mg L^{-1}) recovery during flow desorption of Mg^{2+} from Mg-SQCOF after batch and flow adsorption activity on Li-SQCOF. (d) Mg^{2+} adsorption capacity of Li-SQCOF in a continuous flow adsorption system as a function of permeate volume.

Mg-SQCOFs, and both were treated with HCl at different pH levels (Figure 8b). From the Mg-SQCOF derived from SQCOF, we were able to recover 93% of the adsorbed Mg^{2+}, whereas from the Mg-SQCOF from Li-SQCOF, only 81% of the adsorbed Mg^{2+} was recovered. In both cases, the results indicate that lower pH was more efficient for Mg^{2+} stripping. Conversely, the recovery of Mg^{2+} from Li-SQCOF was slightly less than that from SQCOF, which may be due to the stronger interactions between Mg^{2+} with the more negatively charged Li-SQCOF surface.

3.9. Adsorption and Desorption Studies in Continuous Flow Conditions. After evaluation of the COFs with respect to magnesium adsorption under batch conditions, we extended our investigation to a continuous flow adsorption system. The COF-supported ultrafiltration (CSU) bed for the removal of Mg^{2+} from the Li^+/Mg^{2+} mixture was made by passing a suspension of Li-SQCOF (30 mg) through the cellulose-based Whatman filter paper (Spartan 30/0.22, Figure S2). The solid Li-SQCOF remained on the filter paper, and the ion solutions were passed through the bed using an injection flow pump. The continuous CSU of Mg^{2+} was monitored under various conditions by the following parameters: Mg retention (R_{Mg})[50] and separation flux (F_{Mg}). The separation flux is modified from the permeation flux reported by Chen et al.[51] We have introduced the concentration of the adsorbate and the mass of the adsorbent terms to explain the adsorption under flow conditions. R_{Mg} (%) and F_{Mg} ($m^{-2}h^{-1}$) are defined by eqs (4and 5).

$$R_{Mg}\,(\%) = \left(1 - \frac{C_p}{C_r}\right) * 100 \tag{4}$$

$$F_{Mg} = \frac{\Delta C * V}{A * W * t} \tag{5}$$

where C_p is the concentration (mg L^{-1}) of Mg^{2+} in the permeate, C_r is the concentration (mg L^{-1}) of Mg^{2+} in the retentate, ΔC is the change in the concentration of Mg^{2+} in the permeate before and after filtration ((mg L^{-1})), V is the separation volume (L), A is the effective area of the CSU bed (m^2), W is the mass of COF used, and t is the filtration time (h).

Two Mg^{2+} solutions, 22 mg L^{-1} and 8 mg L^{-1},were passed through the CSU bed, and R_{Mg} and F_{Mg} were calculated and plotted against the volume collected after the CSU bed (Figure 9a). For a concentration of 22 mg L^{-1} of Mg^{2+}, R_{Mg} was 69% at a flux volume of 10 mL, while the F_{Mg} value was 61 h^{-1} m^{-2}. In the same way, the percent removal of Mg^{2+} from the flux volume decreased with the permeation of the solution as expected (Figure 9b). At a lower starting concentration of 8 mg L^{-1} Mg^{2+}, the R_{Mg} was 88% at a flux volume of 10 mL, while the F_{Mg} value was 28 m^{-2} h^{-1}.

After the adsorption of Mg^{2+} in batch and continuous systems, Mg-SQCOFs were individually subjected to flow desorption in HCl (pH 2.0) to evaluate recovery. At an initial flow volume of 10 mL in both systems, 28 and 18 mg L^{-1} Mg^{2+} solutions were recovered quickly, and complete Mg^{2+} recovery was attained after 50 mL of acid solution flowed through the system (Figure 9c).

Li-SQCOF illustrated Mg^{2+} adsorption capacity in the continuous flow adsorption system (Figure 9d). Li-SQCOF has shown 4.85 mg g^{-1} Mg^{2+} adsorption capacity using a 10 mL flow volume of Mg^{2+} solution, which increases to 8.52 mg g^{-1} at a flow volume of 150 mL. A comparison of the Mg^{2+} maximum adsorption capacity (Q_{max}) of SQCOF and Li-SQCOF for Mg^{2+} in different conditions shows very significant and selective Mg^{2+} adsorption in the presence of Li^+, Na^+, and K^+ efficiently both in batch and continuous flow systems (Figure S8).

Powder XRD of SQCOF and Li-SQCOF were taken after Mg^{2+} adsorption and desorption activity cycles by breaking apart the filter and completely drying the COF powders. The results indicate that the SQCOF and Li-SQCOF retain their structure after at least 15 runs and hence could be used for scaling up treatments (Figure S7). A cycle SQCOF was considered as charging with 0.1 M LiOH, followed by separation of mixed Mg^{2+}/Li^+ solutions, and then discharging by treatment with dilute HCl (Figure 10). SQCOF retains 96% of its initial adsorption capacity in the 2nd cycle, whereas it retains 94% of its initial adsorption capacity after 15 cycles, which proves that SQCOF is suitable for long-term use. The results of this study were compared with the other technologies reported in the literature, and SQCOF showed improved removal efficiency of Mg^{2+} from the Li^+/Mg^{2+} mixture combined with a simple, low-cost, low-energy, and environmentally friendly process (Table S3).

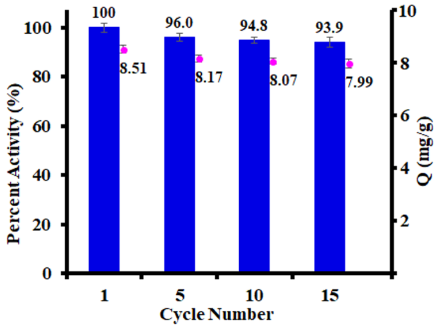

Figure 10. Variation of Mg^{2+} adsorption capacity for Li-SQCOF with recycling the activity; blue columns indicate the percentage of initial adsorption capacity, whereas pink dots indicate the actual values of the adsorption capacity (Q). All of the values are the average of triplicate experiments.

4. CONCLUSIONS

We have synthesized a new COF, SQCOF, which is an active porous material for selectively capturing Mg^{2+} from a mixture of Li^+ and Mg^{2+} ions from water. SQCOF was synthesized by the coupling of squaric acid and 4,4′,4″,4‴-(pyrene-1,3,6,8-tetrayl)-tetraaniline in an n-butanol/o-dichlorobenzene solvent mixture at 85 °C for 7 days. SQCOF was deprotonated using lithium hydroxide to form Li-SQCOF, and both the parent COF and the Li COF are stable at high and low pH levels, retaining their crystallinity with AA stacking. Both SQCOF and Li-SQCOF were efficient enough for Mg^{2+} capturing; however, additional negative charges on the Li-SQCOF surface at higher pH have shown better efficiency to complete removal even in the presence of negligible amounts of Mg^{2+}. It was also observed that the adsorption capacity is dependent on key factors such as the amount of the loaded adsorbent, solution ionic strength, and the amount of the adsorbate. Further, SQCOF and Li-SQCOF are reusable, and they retain their structure and crystallinity even after the removal of Mg^{2+} with HCl in batch as well as flow processes after 15 cycles. Li-SQCOF has shown very significant and selective Mg^{2+} adsorption in continuous flow systems with a high F_{Mg} value of 60.5 h^{-1} m^{-2}. This investigation could open a new window for designing covalent organic frameworks as a sorbent for the removal of Mg^{2+} and purification of Li^+ from natural salt-lake waters.

■ ASSOCIATED CONTENT

Supporting Information

The Supporting Information is available free of charge at https://pubs.acs.org/doi/10.1021/acsami.3c01051.

Additional synthetic details and characterization data; data tables; and comparison information between different COFs and references (PDF)

AUTHOR INFORMATION

Corresponding Author

Alireza Abbaspourrad − *Department of Food Science, College of Agriculture and Life Sciences, Cornell University, Ithaca 14853 New York, United States;* orcid.org/0000-0001-5617-9220; Email: alireza@cornell.edu

Authors

Ataf Ali Altaf − *Department of Food Science, College of Agriculture and Life Sciences, Cornell University, Ithaca 14853 New York, United States*

Ahmadreza Khosropour − *Department of Food Science, College of Agriculture and Life Sciences, Cornell University, Ithaca 14853 New York, United States*

Amin Zadehnazari − *Department of Food Science, College of Agriculture and Life Sciences, Cornell University, Ithaca 14853 New York, United States*

Complete contact information is available at: https://pubs.acs.org/10.1021/acsami.3c01051

Author Contributions

A.A.A.: conceptualization, formal analysis, meth odology investigation, writing—original draft, and writing—review and editing. A.R.K.: supervision and writing—review and editing. A.Z.: investigation and writing—review and editing. A.A.: project administration, resources, funding acquisition, supervision, and writing—review and editing.

Notes

The authors declare no competing financial interest.

ACKNOWLEDGMENTS

The authors acknowledge the Cornell Center for Materials Research (CCMR) for the usage of their services. CCMR facilities are sponsored by the National Science Foundation under grant number DMR-1719875.

REFERENCES

(1) Ding, Y.; Cano, Z. P.; Yu, A.; Lu, J.; Chen, Z. Automotive Li-Ion Batteries: Current Status and Future Perspectives. *Electrochem. Energy Rev.* **2019**, *2*, 1−28.

(2) Lebrouhi, B. E.; Baghi, S.; Lamrani, B.; Schall, E.; Kousksou, T. Critical Materials for Electrical Energy Storage: Li-Ion Batteries. *J. Energy Storage* **2022**, *55*, No. 105471.

(3) Desaulty, A.-M.; Monfort Climent, D.; Lefebvre, G.; Cristiano-Tassi, A.; Peralta, D.; Perret, S.; Urban, A.; Guerrot, C. Tracing the Origin of Lithium in Li-Ion Batteries Using Lithium Isotopes. *Nat. Commun.* **2022**, *13*, No. 4172.

(4) Samadiy, M.; Deng, T. Lithium Recovery from Water Resources by Ion Exchange and Sorption Method. *J. Chem. Soc. Pak.* **2021**, *43*, 406.

(5) Wang, J.; Yue, X.; Wang, P.; Yu, T.; Du, X.; Hao, X.; Abudula, A.; Guan, G. Electrochemical Technologies for Lithium Recovery from Liquid Resources: A Review. *Renewable Sustainable Energy Rev.* **2022**, *154*, No. 111813.

(6) Ighalo, J. O.; Amaku, J. F.; Olisah, C.; Adeola, A. O.; Iwuozor, K. O.; Akpomie, K. G.; Conradie, J.; Adegoke, K. A.; Oyedotun, K. O. Utilisation of Adsorption as a Resource Recovery Technique for Lithium in Geothermal Water. *J. Mol. Liq.* **2022**, *365*, No. 120107.

(7) Liu, G.; Zhao, Z.; He, L. Highly Selective Lithium Recovery from High Mg/Li Ratio Brines. *Desalination* **2020**, *474*, No. 114185.

(8) Stringfellow, W. T.; Dobson, P. F. Technology for the Recovery of Lithium from Geothermal Brines. *Energies* **2021**, *14*, 6805.

(9) Wang, Y.; Liu, H.; Fan, J.; Liu, X.; Hu, Y.; Hu, Y.; Zhou, Z.; Ren, Z. Recovery of Lithium Ions from Salt Lake Brine with a High Magnesium/Lithium Ratio Using Heteropolyacid Ionic Liquid. *ACS Sustainable Chem. Eng.* **2019**, *7*, 3062−3072.

(10) Li, Z.; Mercken, J.; Li, X.; Riaño, S.; Binnemans, K. Efficient and Sustainable Removal of Magnesium from Brines for Lithium/Magnesium Separation Using Binary Extractants. *ACS Sustainable Chem. Eng.* **2019**, *7*, 19225−19234.

(11) Sun, Y.; Wang, Q.; Wang, Y.; Yun, R.; Xiang, X. Recent Advances in Magnesium/Lithium Separation and Lithium Extraction Technologies from Salt Lake Brine. *Sep. Purif. Technol.* **2021**, *256*, No. 117807.

(12) Soyekwo, F.; Wen, H.; Liao, D.; Liu, C. Nanofiltration Membranes Modified with a Clustered Multiquaternary Ammonium-Based Ionic Liquid for Improved Magnesium/Lithium Separation. *ACS Appl. Mater. Interfaces* **2022**, *14*, 32420−32432.

(13) Zhang, C.; Mu, Y.; Zhang, W.; Zhao, S.; Wang, Y. PVC-Based Hybrid Membranes Containing Metal-Organic Frameworks for Li +/Mg2+ Separation. *J. Membr. Sci.* **2020**, *596*, No. 117724.

(14) Li, X.; Hill, M. R.; Wang, H.; Zhang, H. Metal−Organic Framework-Based Ion-Selective Membranes. *Adv. Mater. Technol.* **2021**, *6*, No. 2000790.

(15) Rodríguez-San-Miguel, D.; Montoro, C.; Zamora, F. Covalent Organic Framework Nanosheets: Preparation, Properties and Applications. *Chem. Soc. Rev.* **2020**, *49*, 2291−2302.

(16) Gendy, E. A.; Ifthikar, J.; Ali, J.; Oyekunle, D. T.; Elkhlifia, Z.; Shahib, I. I.; Khodair, A. I.; Chen, Z. Removal of Heavy Metals by Covalent Organic Frameworks (COFs): A Review on Its Mechanism and Adsorption Properties. *J. Environ. Chem. Eng.* **2021**, *9*, No. 105687.

(17) Freund, R.; Zaremba, O.; Arnauts, G.; Ameloot, R.; Skorupskii, G.; Dincă, M.; Bavykina, A.; Gascon, J.; Ejsmont, A.; Goscianska, J.; et al. The Current Status of MOF and COF Applications. *Angew. Chem., Int. Ed.* **2021**, *60*, 23975−24001.

(18) Sajjad, M.; Lu, W. Covalent Organic Frameworks Based Nanomaterials: Design, Synthesis, and Current Status for Supercapacitor Applications: A Review. *J. Energy Storage* **2021**, *39*, No. 102618.

(19) Machado, T. F.; Serra, M. E. S.; Murtinho, D.; Valente, A. J.; Naushad, M. Covalent Organic Frameworks: Synthesis, Properties and Applications—an Overview. *Polymers* **2021**, *13*, 970.

(20) Zhang, Z.; Kang, C.; Peh, S. B.; Shi, D.; Yang, F.; Liu, Q.; Zhao, D. Efficient Adsorption of Acetylene over CO2 in Bioinspired Covalent Organic Frameworks. *J. Am. Chem. Soc.* **2022**, *144*, 14992−14996.

(21) Fan, H.; Mundstock, A.; Feldhoff, A.; Knebel, A.; Gu, J.; Meng, H.; Caro, J. Covalent Organic Framework−Covalent Organic Framework Bilayer Membranes for Highly Selective Gas Separation. *J. Am. Chem. Soc.* **2018**, *140*, 10094−10098.

(22) Kandambeth, S.; Biswal, B. P.; Chaudhari, H. D.; Rout, K. C.; Kunjattu, H. S.; Mitra, S.; Karak, S.; Das, A.; Mukherjee, R.; Kharul, U. K.; Banerjee, R. Selective Molecular Sieving in Self-standing Porous Covalent-organic-framework Membranes. *Adv. Mater.* **2017**, *29*, No. 1603945.

(23) Gong, X.; Zhang, G.; Dong, H.; Wang, H.; Nie, J.; Ma, G. Self-Assembled Hierarchical Heterogeneous MXene/COF Membranes for Efficient Dye Separations. *J. Membr. Sci.* **2022**, *657*, No. 120667.

(24) Wang, R.; Guo, J.; Xue, J.; Wang, H. Covalent Organic Framework Membranes for Efficient Chemicals Separation. *Small Struct.* **2021**, *2*, No. 2100061.

(25) Basel, N.; Liu, Q.; Fan, L.; Wang, Q.; Xu, N.; Wan, Y.; Dong, Q.; Huang, Z.; Guo, T. Surface Charge Enhanced Synthesis of TpEB-Based Covalent Organic Framework (COF) Membrane for Dye Separation with Three Typical Charge Properties. *Sep. Purif. Technol.* **2022**, *303*, No. 122243.

(26) Wang, R.; Wei, M.; Wang, Y. Secondary Growth of Covalent Organic Frameworks (COFs) on Porous Substrates for Fast Desalination. *J. Membr. Sci.* **2020**, *604*, No. 118090.

(27) Zhou, W.; Wei, M.; Zhang, X.; Xu, F.; Wang, Y. Fast Desalination by Multilayered Covalent Organic Framework (COF) Nanosheets. *ACS Appl. Mater. Interfaces* **2019**, *11*, 16847−16854.

(28) Raza, A.; Hassan, J. Z.; Mahmood, A.; Nabgan, W.; Ikram, M. Recent Advances in Membrane-Enabled Water Desalination by 2D Frameworks: Graphene and Beyond. *Desalination* **2022**, *531*, No. 115684.

(29) Xu, R.; Kang, Y.; Zhang, W.; Zhang, X.; Pan, B. Oriented UiO-67 Metal−Organic Framework Membrane with Fast and Selective Lithium-Ion Transport. *Angew. Chem., Int. Ed.* **2022**, *61*, No. e202115443.

(30) Li, J.; Fang, F.; Zhang, Y.; Dai, Z.; Hu, J.; Zhou, Q.; Zhou, G.; Yang, Z. Electric Field-Driven Ultraefficient Li+/Mg2+ Separation through Graphyne Membrane. *Ind. Eng. Chem. Res.* **2022**, *61*, 18080−18089.

(31) Xu, F.; Dai, L.; Wu, Y.; Xu, Z. Li+/Mg2+ Separation by Membrane Separation: The Role of the Compensatory Effect. *J. Membr. Sci.* **2021**, *636*, No. 119542.

(32) Li, W.; Huang, X.; Zeng, T.; Liu, Y. A.; Hu, W.; Yang, H.; Zhang, Y.-B.; Wen, K. Thiazolo[5,4-d]Thiazole-Based Donor−Acceptor Covalent Organic Framework for Sunlight-Driven Hydrogen Evolution. *Angew. Chem., Int. Ed.* **2021**, *60*, 1869−1874.

(33) Ding, N.; Zhou, T.; Weng, W.; Lin, Z.; Liu, S.; Maitarad, P.; Wang, C.; Guo, J. Multivariate Synthetic Strategy for Improving Crystallinity of Zwitterionic Squaraine-Linked Covalent Organic Frameworks with Enhanced Photothermal Performance. *Small* **2022**, *18*, No. 2201275.

(34) Yum, J.-H.; Walter, P.; Huber, S.; Rentsch, D.; Geiger, T.; Nüesch, F.; De Angelis, F.; Grätzel, M.; Nazeeruddin, M. K. Efficient Far Red Sensitization of Nanocrystalline TiO2 Films by an Unsymmetrical Squaraine Dye. *J. Am. Chem. Soc.* **2007**, *129*, 10320−10321.

(35) López, C.; Vega, M.; Sanna, E.; Rotger, C.; Costa, A. Efficient Microwave-Assisted Preparation of Squaric Acid Monoamides in Water. *RSC Adv.* **2013**, *3*, 7249−7253.

(36) Mejuch, T.; Garivet, G.; Hofer, W.; Kaiser, N.; Fansa, E. K.; Ehrt, C.; Koch, O.; Baumann, M.; Ziegler, S.; Wittinghofer, A.; Waldmann, H. Small-Molecule Inhibition of the UNC119−Cargo Interaction. *Angew. Chem., Int. Ed.* **2017**, *56*, 6181−6186.

(37) Xie, J.; Comeau, A. B.; Seto, C. T. Squaric Acids: A New Motif for Designing Inhibitors of Protein Tyrosine Phosphatases. *Org. Lett.* **2004**, *6*, 83−86.

(38) Ximenis, M.; Bustelo, E.; Algarra, A. G.; Vega, M.; Rotger, C.; Basallote, M. G.; Costa, A. Kinetic Analysis and Mechanism of the Hydrolytic Degradation of Squaramides and Squaramic Acids. *J. Org. Chem.* **2017**, *82*, 2160−2170.

(39) Neuse, E. W.; Green, B. R. Dianilino Derivatives of Squaric Acid. *J. Org. Chem.* **1974**, *39*, 3881−3887.

(40) Prabhakar, Ch.; Bhanuprakash, K.; Rao, V. J.; Balamuralikrishna, M.; Rao, D. N. Third Order Nonlinear Optical Properties of Squaraine Dyes Having Absorption below 500 Nm: A Combined Experimental and Theoretical Investigation of Closed Shell Oxyallyl Derivatives. *J. Phys. Chem. C* **2010**, *114*, 6077−6089.

(41) Nagai, A.; Chen, X.; Feng, X.; Ding, X.; Guo, Z.; Jiang, D. A Squaraine-Linked Mesoporous Covalent Organic Framework. *Angew. Chem., Int. Ed.* **2013**, *52*, 3770−3774.

(42) Ding, N.; Zhou, T.; Weng, W.; Lin, Z.; Liu, S.; Maitarad, P.; Wang, C.; Guo, J. Multivariate Synthetic Strategy for Improving Crystallinity of Zwitterionic Squaraine-Linked Covalent Organic Frameworks with Enhanced Photothermal Performance. *Small* **2022**, *18*, No. 2201275.

(43) Villarroel-Rocha, J.; Barrera, D.; Arroyo-Gómez, J. J.; Sapag, K. Critical Overview of Textural Characterization of Zeolites by Gas Adsorption. In *New Developments in Adsorption/Separation of Small Molecules by Zeolites: Structure and Bonding*; Valencia, S.; Rey, F., Eds.; Springer International Publishing: Cham, 2020; pp 31−55 DOI: 10.1007/430_2020_69.

(44) Guo, X.; Zhang, X.; Zhao, S.; Huang, Q.; Xue, J. High Adsorption Capacity of Heavy Metals on Two-Dimensional MXenes: An Ab Initio Study with Molecular Dynamics Simulation. *Phys. Chem. Chem. Phys.* **2016**, *18*, 228−233.

(45) Adamson, A. W.; Gast, A. P. *Physical Chemistry of Surfaces*; Interscience publishers: New York, 1967; Vol. *150*.

(46) Ceyer, S. T. New Mechanisms for Chemistry at Surfaces. *Science* **1990**, *249*, 133−139.

(47) Razmjou, A.; Asadnia, M.; Hosseini, E.; Habibnejad Korayem, A.; Chen, V. Design Principles of Ion Selective Nanostructured Membranes for the Extraction of Lithium Ions. *Nat. Commun.* **2019**, *10*, No. 5793.

(48) Rao, S. N. Chapter 5 - Adsorption. In *Interface Science and Technology*; Ball, V., Ed.; Elsevier, 2018; Vol. *21*, pp 251−331 DOI: 10.1016/B978-0-12-801970-2.00005-7.

(49) Bullen, J. C.; Saleesongsom, S.; Gallagher, K.; Weiss, D. J. A Revised Pseudo-Second-Order Kinetic Model for Adsorption, Sensitive to Changes in Adsorbate and Adsorbent Concentrations. *Langmuir* **2021**, *37*, 3189−3201.

(50) Rether, A.; Schuster, M. Selective Separation and Recovery of Heavy Metal Ions Using Water-Soluble N-Benzoylthiourea Modified PAMAM Polymers. *React. Funct. Polym.* **2003**, *57*, 13−21.

(51) Chen, Y.; Chen, L.; Lu, C.; Wang, L.; Dong, L.; Zhou, C.; Huang, X. A COFs-Coated Polyamide Membrane Fabricated by Vapor-Assisted Conversion for Water-in-Oil Emulsions Separation. *New J. Chem.* **2022**, *46*, 22889−22894.